PERGAMON

International Journal of Heat and Mass Transfer 43 (2000) 1007–1023

International Journal of HEAT and MASS TRANSFER

www.elsevier.com/locate/ijhmt

Combined evaporating meniscus-driven convection and radiation in annular microchannels for electronics cooling application

C.P. Tso*, S.P. Mahulikar

School of Mechanical and Production Engineering, Nanyang Technological University, Nanyang Avenue, Singapore 639798, Singapore

Received 4 January 1999; received in revised form 6 May 1999

Abstract

Surface radiation interchange in an annular enclosure is numerically modeled together with evaporating meniscus-driven convection, for investigating the application of the concept for cooling in microelectronic devices. The geometry is axially discretised into ring elements, where the wall and fluid temperatures within each element are unknowns. The governing algebraic energy equations for convection and surface radiation for each element are formulated for steady-state operating conditions for heat generating cylinders. These equations are then solved simultaneously for all the elements, together with the integral form of the momentum equation, which equates the driving force due to the meniscus curvature to the weight of the coolant and the frictional resistance, and solely dictates the coolant rise length in the microchannel. The results reveal the coupling of fluid flow and heat transfer in the annular microchannel, and the relative importance of radiation.

Keywords: Electronics cooling; Meniscus-driven convection; Microchannel cooling; Radiation

1. Introduction

The trend of miniaturisation in computer technology has resulted in increased packaging flux densities as in very-large-scale integration (VLSI) and wafer-scale integration (WSI), which has significantly increased the problems associated with overheating of integrated circuit (IC) chips [1]. The conventional means of heat dissipation by natural and forced convection are no longer satisfactory solutions, which has resulted in an unprecedented upsurge of interests in microscale heat transfer. Also, the efficient heat transfer provided by phase change has long been recognised as a superior cooling technique. Recently, applications utilising phase change of the coolant have been developed, which has led to investigations involving phase change in close proximity to the chip surface [2,3].

The experiments of Peng and Wang [4] indicated that the flow boiling characteristics of subcooled liquid flowing through microchannels with a cross-section of 0.6×0.7 mm differ significantly from those in the conventionally sized. No partial nucleate boiling of the subcooled liquid was observed for the transition from single-phase liquid to nucleate boiling, and the fully developed boiling was found to be induced much earlier. However, even for this fully developed nucleate boiling region, no bubbles were observed. This implied

* Corresponding author. Tel.: +65-7995033; fax: +65-7911859.

E-mail address: mcptso@ntu.edu.sg (C.P. Tso).

0017-9310/00/$ - see front matter
PII: S0017-9310(99)00186-6

Nomenclature

A	surface area of cylinder wall m^2
B	radiosity W/m^2
C	specific heat (J/kg K)
C_f	friction coefficient in Eq. (10.2)
d	annular microchannel spacing (m)
D	cylinder diameter (m)
D_h	hydraulic diameter of microchannel (m)
f	friction factor based on pressure drop
F_{i-j}	view factor of surface j as seen by surface i
g	acceleration due to gravity (m/s^2)
h	convective heat transfer coefficient (W/m^2 K)
H	irradiation (W/m^2)
k	thermal conductivity of coolant (W/m K)
Kn	Knudsen number, λ/d
L	length of cylinders (m)
L_H	latent heat of vapourisation of coolant (J/kg)
L_r	coolant rise length in annular microchannel (m)
$\dot{m}$	mass flow rate (kg/s)
M	molecular weight of annulus coolant (kg/mole)
n	number of molecules per unit volume (m^{-3})
N	number of elements in which configuration is discretised
Nu	Nusselt number, hD_h/k
ΔP_{lv}	pressure difference at liquid–vapour interface of evaporating meniscus (Pa)
$\dot{q}''$	heat flux (W/m^2)
$\dot{Q}'''$	volume heat generation rate of cylinder (W/m^3)
R_1, R_2	principal radii of curvature in Young–Laplace equation (m)
R_c	capillary radius (m)
Re	Reynolds number
t	thickness of cylinder (m)
T	temperature (K)
V	velocity (m/s)
x	distance measured along axis of coaxial cylinders (m)
ε	emissivity of surface
ϕ	diameter of molecule (m)
η	surface tension of coolant (N/m)
λ	mean free path of molecules (m)
θ	inclination of axis of coaxial cylinders (deg)
ρ	coolant density (kg/m^3)
σ	Stefan–Boltzmann constant (W/m^2 K^4)
Ω	volume associated with one molecule (m^3)

Subscripts

a	air flowing inside inner cylinder
cl	liquid coolant flowing in annular passage due to evaporating meniscus
cv	convection
D	based on diameter
ed	annular disc at exit to annular passage
i	inner surface of cylinder
id	annular disc at inlet to annular passage
in	value at inlet
K, K'	referring to Kth, K'th element of discretised configuration, where K, $K' < N$
max	maximum value
N	Nth element
o	outer surface of cylinder
p	at constant pressure
rd	radiation
s	shell
sat	saturation value
si	shell interior surface (Fig. 3)
t	tube
te	tube exterior surface (Fig. 3)
v	coolant vapour flowing in annular passage after evaporating meniscus
w1, w2	inner (1), outer (2) cylinder walls
∞	ambient/freestream conditions

that bubble growth in the liquid might be related to the scale of the liquid bulk, referred to as the evaporation scale or space, which is the minimum space necessary for evaporation. Their results showed the Reynolds number as not very important in microchannels compared to the capillary force, for $Re < 3000$. The experiments of Peng et al. [5] with phase change showed that with a sufficiently high superheat, flow boiling was initiated at once and immediately developed into fully developed nucleate boiling. Hence, though the liquid subcooling was sufficiently high, apparent partial nucleate regime was not found to exist, as reported earlier by Peng and Wang. They attributed the enhancement of the heat removal rate to this rapid change to the fully developed nucleate flow boiling, and concluded that in microchannels the nucleate boiling is intensified, and the wall surface superheat for flow boiling may be significantly smaller than in the conventionally sized channels for a given wall heat flux.

Peng et al. [6] analysed the thermodynamic aspects of phase transformation of liquids in microchannels to appreciate the boiling characteristics, and to determine the conditions under which a portion of the liquid may

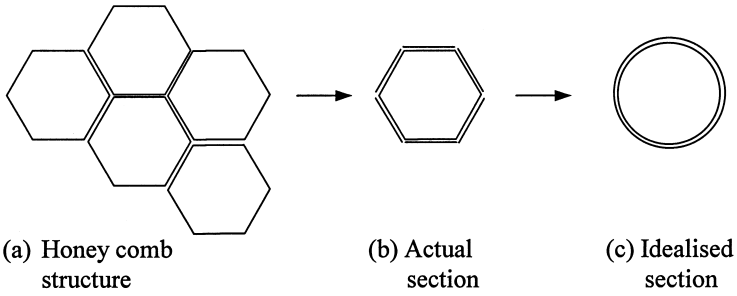

Fig. 1. Sections of arrangements of IC chips: (a) honey comb structure; (b) actual section; (c) idealised section.

undergo phase change. Their analysis showed that nucleation is related to the applied heat flux, the thermophysical properties of the liquid, and the hydraulic diameter (D_h) of the microchannels. The small size of the microchannels was found to result in dramatically high heat fluxes and superheats for liquid nucleation. The minimum heat flux needed to induce phase transition or nucleation was found to increase rapidly as D_h decreased for a specified liquid. Their theoretical evidences also demonstrated that a single-phase liquid flowing in microchannels absorbs extraordinarily high heat fluxes, which are higher than those for nucleate boiling in the conventionally sized channels. They concluded that the liquid is in a highly non-equilibrium state with a high capacity to absorb, transfer, and transport thermal energy. Their analysis supported the hypothetical concepts of 'evaporating space', introduced in [4], and 'fictitious boiling', the latter referring to the liquid that has reached conventional nucleate boiling conditions, but without internal evaporation and bubble growth. Thus, the survey on phase change in microchannels indicates that since bubbles are generally not formed, the liquid is in a state of non-equilibrium in the saturated liquid phase after conventional nucleate boiling conditions have been realised. Hence, phase change occurs only from the surface of the evaporating meniscus.

Several authors analysed the intrinsic and extended evaporating meniscus in isolation. For instance, Moosman and Homsy [7] mathematically modeled the transport processes in a horizontal-evaporating meniscus, affected by capillarity (in the intrinsic meniscus) and multilayer adsorption (in the extended meniscus). Dasgupta et al. [8] evaluated the experimental data for the extended portion of the meniscus, using numerical solutions of equilibrium and non-equilibrium models based on the augmented Young–Laplace equation. Hallinan et al. [9] studied the effects of evaporation from the non-equilibrium portion of the extended meniscus on the interfacial shape, temperature, and pressure distribution.

The survey on evaporating meniscus indicates that coupled fluid mechanics and heat transfer in an isolated evaporating meniscus has been studied in details in the intrinsic and extended portions of the meniscus. However, there is a lack of studies on the coupled multimode heat transfer and liquid flow, upstream of the evaporating meniscus. This is probably because the role played by the evaporating meniscus during phase change in microchannels, and the significance of it coupling the heat transfer and fluid flow upstream, were yet to be identified. The evaporating meniscus causes this coupling, whenever there is phase change in closed microchannels. The present study numerically analyses the heat transfer in the immersion-cum-microchannel direct cooling technique in an annular microchannel formed between two coaxial heat generating cylinders. The annular microchannel idealises a three-dimensional (3D) hexagonal package of IC chips or circuit boards in a honeycomb arrangement with microscale spacing between adjacent hexagonal units (Fig. 1). The components are arranged such that the electrically active face is the interior of the hexagon, and the electrically inactive face is the exterior of the hexagon. Fig. 1(a) shows the honey comb arrangement, Fig. 1(b) shows a unit of this arrangement, and Fig. 1(c) shows the idealised unit to be used for numerical modeling. The technique of evaporating meniscus-driven flow was introduced by Tso and Mahulikar [10], and uses the capillary force due to the curvature of the evaporating meniscus for driving the coolant in the microchannel. It combines the benefits of high value of the forced convection coefficient in microchannels, mentioned, for instance, in [4,11], and phase change of the liquid coolant. As only one side of the IC (the electrically inactive face) is in direct contact with the coolant, the requirement of the coolant to be dielectric is relaxed.

A model is presented in [10], simulating the evaporating meniscus-driven coolant flow in a rectangular microchannel formed between two parallel flat plates; one of which is heated and the other insulated, thus idealising a 2D package of IC chips. Results were obtained for the variation of the coolant rise length,

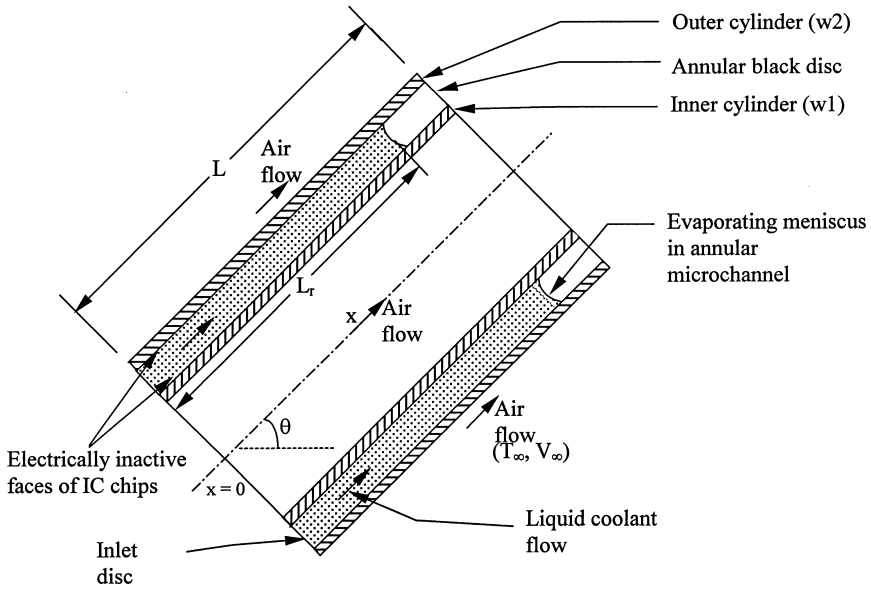

Fig. 2. Schematic sketch of evaporating meniscus-driven coolant flow in annular microchannel.

velocity, and capillary number, for various coolants, heat fluxes, and microchannel inclinations. The technique was extended to an idealised 3D IC package in which a similar approach was applied to an annular microchannel bound by two heat generating cylinders [12,13]. In these studies [10,12,13], the friction coefficient used in the momentum equation was that for a conventionally sized channel. Hence, the coolant rise length varied with heat flux, since the rise length is not solely dictated by the integral form of the momentum equation. In Ref. [14], a numerical study of the same configuration was performed with the friction factor of that for a microchannel, obtained from [15].

In none of the above studies were radiation effects included. However, in microscale flow passages, radiation interchange among surfaces may be important due to the inverse square law dependence of radiation, which may hold in spite of the relatively low temperatures for reliable chip operation. In the annular microchannel, gas radiation is not likely to be of significance, since the mean beam length is small. The discretised annular enclosure gives ring elements on tube exterior and shell interior surfaces, necessitating the estimation of finite view factors between tube exterior to shell interior surfaces, shell interior to shell interior surfaces, and between tube exterior and shell interior surfaces to end-plugged annular discs at the inlet and exit. Howell [16] has provided an analytical solution for the view factor from the exterior surface of a coaxial cylinder of smaller radius to the interior surface of a coaxial cylinder of larger radius (Configuration C-93 in [16]), and has also provided the numerical results of Reid and Tennant [17] for the view factor between tube exterior and shell interior surfaces (Configuration C-95 in [16]). The view factors for Configurations C-93 and C-95 in [16] have been explicitly shown identical by Tso and Mahulikar [18]. They have also derived the analytical expressions for the view factors between finite shell interior surfaces [19]. Rea [20] outlined the view factor algebra for obtaining the view factor from the outer cylindrical surface of smaller radius to the inner cylindrical surface of larger radius. Brockmann [21] provided simplified expressions for the known view factors between shell interior to shell interior surfaces, and between shell interior to tube exterior surfaces of equal lengths.

In the present work, the idealised 3D IC package consisting of several ICs to be cooled together is numerically simulated. The governing equations for the discretised configuration are obtained for each element, and solved numerically. Surface radiation is modeled by the radiosity–irradiation approach, with all required view factors obtained analytically. The radiation energy equations are solved together with the convection equations for the coolants under steady state. Based on the findings as surveyed earlier that bubbles are not formed in microchannels and the liquid coolant is in a state of non-equilibrium, the microchannel coolant is assumed to be saturated liquid upon reaching the saturation temperature till the complete latent heat is supplied to the coolant.

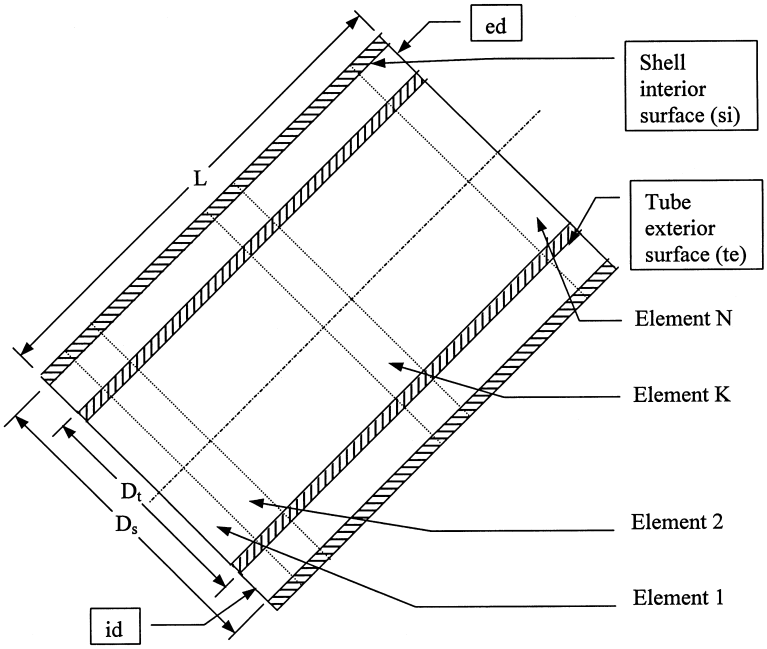

Fig. 3. Discretisation of configuration for heat transfer modeling.

2. Problem formulation

Fig. 1 shows a section of a compact arrangement of a group of IC chips to be cooled together. The chips are arranged in the form of two regular concentric polygons, with the electrically inactive faces facing each other. If the number of chips is large, they are positioned one above the other. The chips to be cooled to a higher degree (high heat generating chips) are placed at the bottom (i.e. the chips are placed from bottom to top in the descending order of their cooling requirement). Fig. 2 shows the schematic sketch of the idealised configuration comprising of the meniscus-driven coolant flow in the annular microchannel. The easiest way to achieve the configuration shown is by dipping the arrangement in a coolant reservoir. Due to the microscale gap between the two cylinders, the coolant rises due to the small curvature of the meniscus in the annular microchannel, assuming it properly wets the walls of the cylinders. However, there is insignificant coolant rise in the core cylinder since the inner cylinder's inner diameter (D_{1i}) is conventionally sized. Also the coolant rise on the exterior surface of the outer cylinder is insignificant, due to large mass of the unbounded coolant. Hence, the heat transfer from the inner surface of the inner cylinder and the outer surface of the outer cylinder is by natural convection air-flow or forced convection air-flow at a low velocity. Thus the electrically active faces of the chips are cooled by air, which is a dielectric coolant. The annulus coolant cools the electrically inactive faces of the chips, and its temperature rises from the inlet value ($T_{cl,in}$) to the saturation value ($T_{cl,sat}$) at the meniscus due to the heat transferred from the chips. Due to evaporation at the meniscus, there is continuous coolant flow in the annular microchannel. A complete system will also comprise of a condensing unit at the exit of the annular microchannel, which will also protect live electronic components from direct exposure to water vapour. However, the present paper only models the multimode heat transfer in the evaporator section, in order to obtain the temperature distributions, for simulating the performance of the technique.

In the present model, volume heat generation is used rather than a specified wall heat flux, since heat generation is even more fundamental. It is the volumetric heat generation rate that is distributed as the wall heat flux on the two faces, depending upon the thermal resistances. Due to the microscale gap between the two cylinders, radiation interchange between the outer surface of cylinder (w1) and the inner surface of cylinder (w2) might become important, especially when the heat generation rates of the two cylinders significantly differ. Hence, radiation interchange is modeled in the annular enclosure bounded by the surfaces of the cylinders, and the fictitious end-plugged annular disc sur-

faces. The cylinder surfaces and the inlet annular disc surface are assumed to be diffuse, grey, and opaque, while the exit annular disc surface is assumed to be a black body at the ambient temperature. Surface radiation is not considered within cylinder 1 since D_{1i} is conventionally sized. Radiation loss from the outer surface of cylinder 2 is not considered, since its temperature is not high enough. The annulus coolant and air are assumed to be non-participating in radiation.

Also, heat conduction in the axial direction in the cylinders is neglected assuming small thickness of the cylinders compared to length, resulting in large thermal resistance in the axial direction than in the radial direction. The temperature drop in the radial direction due to heat conduction is neglected assuming the Biot number of the cylinders to be much smaller than unity.

The following additional assumptions are made to focus on the significant effects:

1. The coolant completely wets the cylinder walls, irrespective of the channel inclination. This defines the meniscus curvature as

$$R_1 = R_c = \frac{(D_{2i} - D_{1o})}{2}. \tag{1}$$

2. The liquid–vapour pressure difference at the evaporating meniscus, ΔP_{lv}, is a constant throughout the meniscus (though R_2 varies from $D_{1o}/2$ to $D_{2i}/2$). Hence, the mean value of R_2 is used, viz.,

$$R_2 = \frac{(D_{2i} + D_{1o})}{4}. \tag{2}$$

3. The heat generation rates are high enough to evaporate the coolant before reaching the maximum possible rise $L_{r,max}$ (the rise when all the ICs are off), which is given by

$$L_{r,max} = \frac{\Delta P_{lv}}{(\rho_{cl} - \rho_v) \cdot g \cdot \sin\theta}, \tag{3.1}$$

where [22]

$$\Delta P_{lv} = \eta\left(\frac{1}{R_1} + \frac{1}{R_2}\right). \tag{3.2}$$

4. The velocities of the coolant and air are small enough for their flows to be laminar.
5. The fluid temperatures in the equations below are their bulk mean values.

Since an analytical solution is difficult due to the combined radiation and convection heat exchange, and the coupling of heat transfer with fluid flow due to the evaporating meniscus, the geometry is discretised into N ring elements as shown in Fig. 3. As $N\to\infty$, the results of the analytical solution are approached. To enable discretisation, assumptions are made that: the number of chips within an element is a natural number, the heat flux distribution is axisymmetric and constant within an element, and the flows are fully developed. The various parameters and fluid properties governing the heat exchange and flow are variables. Within each element there are $4N$ unknown temperatures, viz., the N temperatures of air flowing inside cylinder 1 ($T_{a1}, T_{a2}, \ldots, T_{aN}$), N temperatures of cylinder 1 ($T_{w1,1}, T_{w1,2}, \ldots, T_{w1,N}$), N temperatures of the annular microchannel coolant flow ($T_{cl,1}, T_{cl,2}, \ldots, T_{cl,N}$), and N temperatures of cylinder 2 ($T_{w2,1}, T_{w2,2}, \ldots, T_{w2,N}$). The Kth element is shown separately along with the convective and radiative heat fluxes in Fig. 4. The radiative heat fluxes are shown in arbitrary direction to represent the multi-directional nature of radiation (unlike convection). Further, it is assumed that the radiosity from the surface of an element and the irradiation on the surface of an element are constant along the elemental surface. This assumption does not directly follow from the assumption of constant surface temperature of an element (made tacitly earlier while assigning variables), since constant surface temperature does not necessarily imply constant irradiation and hence constant radiosity. However, as $N\to\infty$, i.e., when $L/N\to 0$, constant element temperature also implies constant irradiation on and from an elemental surface and hence constant radiosity.

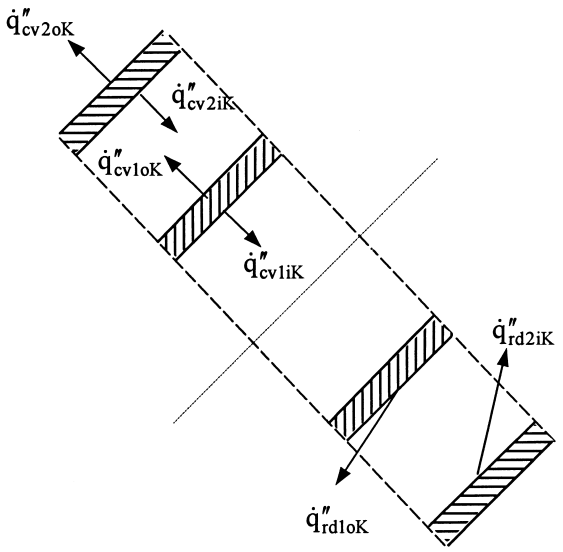

Fig. 4. Heat fluxes in Kth element.

For each discretised element, the governing algebraic energy equations are obtained as below. Eqs. (4.1) and (4.2) state that the heat generated is the heat lost,

$$\dot{q}''_{\mathrm{cv1i}K}\cdot A_{\mathrm{1i}K}+\left(\dot{q}''_{\mathrm{cv1o}K}+\dot{q}''_{\mathrm{rd1o}K}\right)\cdot A_{\mathrm{1o}K}$$
$$=\dot{Q}'''_{1K}\cdot\frac{\pi}{4}\cdot\left(D^2_{\mathrm{1o}}-D^2_{\mathrm{1i}}\right)\cdot\frac{L}{N},\tag{4.1}$$

$$\left(\dot{q}''_{\mathrm{cv2i}K}+\dot{q}''_{\mathrm{rd2i}K}\right)\cdot A_{\mathrm{2i}K}+\dot{q}''_{\mathrm{cv2o}K}\cdot A_{\mathrm{2o}K}$$
$$=\dot{Q}'''_{2K}\cdot\frac{\pi}{4}\cdot\left(D^2_{\mathrm{2o}}-D^2_{\mathrm{2i}}\right)\cdot\frac{L}{N}.\tag{4.2}$$

The convective heat transfer rates are given by the definition as

$$\dot{q}''_{\mathrm{cv1i}K}=h_{\mathrm{1i}K}\cdot\left(T_{\mathrm{w1},K}-T_{\mathrm{a}K}\right),\tag{5.1}$$

$$\dot{q}''_{\mathrm{cv1o}K}=h_{\mathrm{1o}K}\cdot\left(T_{\mathrm{w1},K}-T_{\mathrm{cl},K}\right),\tag{5.2}$$

$$\dot{q}''_{\mathrm{cv2i}K}=h_{\mathrm{2i}K}\cdot\left(T_{\mathrm{w2},K}-T_{\mathrm{cl},K}\right),\tag{5.3}$$

$$\dot{q}''_{\mathrm{cv2o}K}=h_{\mathrm{2o}K}\cdot\left(T_{\mathrm{w2},K}-T_{\infty}\right).\tag{5.4}$$

The convective heat transfer coefficient, $h_{\mathrm{1i}K}$, for fully developed internal flow through a conventionally sized duct is given by $Nu_D=4.36364$ [23], assuming the constant wall heat flux boundary condition. The values of $h_{\mathrm{1o}K}$ and $h_{\mathrm{2i}K}$, which are the convective heat transfer coefficients in the annular microchannel, are obtained from the typical values of Nu taken as 0.4828, which is the mean of the experimentally obtained Nu values for microchannels [24]. The convective heat transfer coefficient, $h_{\mathrm{2o}K}$, for external flow over a cylinder is obtained from the conventional correlation for laminar flow over a flat plate [25]. The sensible enthalpy change of the fluids in passing from one element to the next are given by

$$\dot{q}''_{\mathrm{cv1i}K}\cdot A_{\mathrm{1i}K}=\dot{m}_{\mathrm{a}}\cdot C_{\mathrm{pa}}\cdot\left[T_{\mathrm{a}K}-T_{\mathrm{a}(K-1)}\right],\tag{6.1}$$

and

$$\dot{q}''_{\mathrm{cv1o}K}\cdot A_{\mathrm{1o}K}+\dot{q}''_{\mathrm{cv2i}K}\cdot A_{\mathrm{2i}K}$$
$$=\dot{m}_{\mathrm{cl}}\cdot C_{\mathrm{cl}}\cdot\left[T_{\mathrm{cl},K}-T_{\mathrm{cl},(K-1)}\right].\tag{6.2}$$

Phase change is modeled by keeping the value of $T_{\mathrm{cl},K}$ constant ($=T_{\mathrm{cl,sat}}$) once it increases to $T_{\mathrm{cl,sat}}$, until the complete latent heat ($\dot{m}_{\mathrm{cl}}\cdot L_H$) is supplied, after which single phase convection due to the vapour flow is modeled by using the properties of the vapour in Eq. (6.2).

The radiative heat fluxes from the surfaces of the Kth element are given by

$$\dot{q}''_{\mathrm{rd1o}K}=B_{\mathrm{1o}K}-H_{\mathrm{1o}K},\tag{7.1}$$

and

$$\dot{q}''_{\mathrm{rd2i}K}=B_{\mathrm{2i}K}-H_{\mathrm{2i}K},\tag{7.2}$$

where the radiosities from the elemental surfaces are given by

$$B_{\mathrm{1o}K}=\varepsilon_{\mathrm{1o}K}\cdot\sigma\cdot T^4_{\mathrm{w1},K}+(1-\varepsilon_{\mathrm{1o}K})\cdot H_{\mathrm{1o}K},\tag{7.3.1}$$

and

$$B_{\mathrm{2i}K}=\varepsilon_{\mathrm{2i}K}\cdot\sigma\cdot T^4_{\mathrm{w2},K}+(1-\varepsilon_{\mathrm{2i}K})\cdot H_{\mathrm{2i}K}.\tag{7.3.2}$$

In Eqs. (7.3.1) and (7.3.2), the term $(1-\varepsilon)$ is regarded as the reflectivity of the surfaces. The irradiations on the surfaces of the Kth element are given by

$$H_{\mathrm{1o}K}=F_{\mathrm{1o}K-\mathrm{id}}\cdot B_{\mathrm{id}}+F_{\mathrm{1o}K-\mathrm{2i1}}\cdot B_{\mathrm{2i1}}+\cdots$$
$$+F_{\mathrm{1o}K-\mathrm{2i}N}\cdot B_{\mathrm{2i}N}+F_{\mathrm{1o}K-\mathrm{ed}}\cdot\sigma\cdot T^4_{\infty},\tag{7.3.3}$$

and

$$H_{\mathrm{2i}K}=F_{\mathrm{2i}K-\mathrm{id}}\cdot B_{\mathrm{id}}+F_{\mathrm{2i}K-\mathrm{2i1}}\cdot B_{\mathrm{2i1}}+F_{\mathrm{2i}K-\mathrm{1o1}}$$
$$\cdot B_{\mathrm{1o1}}+\cdots+F_{\mathrm{2i}K-\mathrm{2i}N}\cdot B_{\mathrm{2i}N}+F_{\mathrm{2i}K-\mathrm{1o}N}$$
$$\cdot B_{\mathrm{1o}N}+F_{\mathrm{2i}K-\mathrm{ed}}\cdot\sigma\cdot T^4_{\infty}.\tag{7.3.4}$$

The view factors, $F_{\mathrm{1o}K-\mathrm{id}}$ and $F_{\mathrm{1o}K-\mathrm{ed}}$ are from tube exterior surface to end-plugged inlet and exit discs, respectively; $F_{\mathrm{2i}K-\mathrm{id}}$ and $F_{\mathrm{2i}K-\mathrm{ed}}$ are from shell interior surface to end-plugged inlet and exit discs, respectively; $F_{\mathrm{1o}K-\mathrm{2i}K'}$ are from tube exterior to shell interior surfaces; and $F_{\mathrm{2i}K-\mathrm{2i}K'}$ are from one shell interior surface to another in the presence of the obstructing tube. The individual characters in the subscripts for the view factor are explained in the nomenclature.

Eqs. (4.1), (4.2), (5.1)–(5.4), (6.1), (6.2), (7.1), (7.2), (7.3.1)–(7.3.4), are 14 non-linear simultaneous equations for each element in the following 14 unknowns: $\dot{q}''_{\mathrm{cv1i}K}$, $\dot{q}''_{\mathrm{cv1o}K}$, $\dot{q}''_{\mathrm{cv2i}K}$, $\dot{q}''_{\mathrm{cv2o}K}$, $\dot{q}''_{\mathrm{rd1o}K}$, $\dot{q}''_{\mathrm{rd2i}K}$, $T_{\mathrm{w1},K}$, $T_{\mathrm{w2},K}$, $T_{\mathrm{a}K}$, $T_{\mathrm{cl},K}$, $B_{\mathrm{1o}K}$, $B_{\mathrm{2i}K}$, $H_{\mathrm{1o}K}$, and $H_{\mathrm{2i}K}$. In the phase change region, $T_{\mathrm{cl},K}=T_{\mathrm{cl,sat}}$, hence one equation and one unknown are reduced. However, in the above system of equations, the annulus coolant mass flow rate ($\dot{m}_{\mathrm{cl}}$) is an unknown, since it is coupled with the heat transfer. Also, since the radiation interchange in the annular enclosure is coupled with the grey disc at the inlet, B_{id} and H_{id} are unknowns. Hence, in addition to the above equations for each element, additional equations are included for closing the system. The radiosity from the inlet annular disc is

$$B_{\mathrm{id}}=\varepsilon_{\mathrm{id}}\cdot\sigma\cdot T^4_{\mathrm{id}}+(1-\varepsilon_{\mathrm{id}})\cdot H_{\mathrm{id}}.\tag{8.1}$$

The irradiation on the annular disc at the inlet is given by

$$H_{id} = F_{id-2i1}\cdot B_{2i1} + F_{id-1o1}\cdot B_{1o1} + \cdots + F_{id-2iN}\cdot B_{2iN} + F_{id-1oN}\cdot B_{1oN} + F_{id-ed}\cdot\sigma\cdot T_{\infty}^{4}. \quad (8.2)$$

The view factor F_{id-ed} is between the end-plugged inlet and exit disc surfaces, the view factors F_{id-1oK} are from the end-plugged inlet disc to the tube exterior surface, and F_{id-2iK} are from the end-plugged inlet disc to the shell interior surface in the presence of the obstructing tube.

Thus $(3N^2+6N+1)$ view factors are required. The following pairs of view factors are related by the reciprocal rule: (F_{id-1oK}, F_{1oK-id}), (F_{id-2iK}, F_{2iK-id}), $(F_{1oK-2iK'}, F_{2iK-1oK'})$. Hence, the number of view factors to be determined reduces to $(2N^2+4N+1)$. However, the configurations for the pairs of view factors (F_{1oK-id}, F_{1oK-ed}) and (F_{2iK-id}, F_{2iK-ed}) are identical, thereby reducing the number of configurations for which view factors are required to $(2N^2+2N+1)$, which are F_{id-ed}, F_{id-1oK}, F_{id-2iK}, $F_{1oK-2iK'}$, and $F_{2iK-2iK'}$. The simplified expressions for the view factors F_{si-si} and F_{si-te} (Fig. 3) have been provided in [21] as

$$F_{si-si} = \frac{1}{\pi\Delta_s}\left[\pi(\Delta_s-\Delta_t) + \cos^{-1}\left(\frac{\Delta_t}{\Delta_s}\right) - \sqrt{1+4{\Delta_s}^2} \times \tan^{-1}\frac{\sqrt{\left[1+4{\Delta_s}^2\right]\left[{\Delta_s}^2-{\Delta_t}^2\right]}}{\Delta_t} + 2\Delta_t\cdot\tan^{-1}\left(2\sqrt{{\Delta_s}^2-{\Delta_t}^2}\right)\right] \quad (9.1)$$

$$F_{si-te} = \frac{1}{\pi\Delta_s}\left[\frac{1}{2}\left({\Delta_s}^2-{\Delta_t}^2-1\right)\cos^{-1}\left(\frac{\Delta_t}{\Delta_s}\right) + \pi\Delta_t - \frac{\pi}{2}\left({\Delta_s}^2-{\Delta_t}^2\right) - 2\Delta_t\cdot\tan^{-1}\sqrt{{\Delta_s}^2-{\Delta_t}^2} + \sqrt{\left[1+(\Delta_s+\Delta_t)^2\right]\left[1+(\Delta_s-\Delta_t)^2\right]}\tan^{-1} \times \sqrt{\frac{\left[1+(\Delta_s+\Delta_t)^2\right]\left[\Delta_s-\Delta_t\right]}{\left[1+(\Delta_s-\Delta_t)^2\right]\left[\Delta_s+\Delta_t\right]}}\right], \quad (9.2)$$

where $\Delta_s = D_s/(2L)$ and $\Delta_t = D_t/(2L)$. For the annular enclosure in Fig. 3,

$$F_{si-si} + F_{si-te} + F_{si-id} + F_{si-ed} = 1. \quad (9.3.1)$$

Also, by symmetry,

$$F_{si-id} = F_{si-ed}. \quad (9.3.2)$$

From Eqs. (9.3.1) and (9.3.2),

$$F_{si-id} = \frac{(1-F_{si-si}-F_{si-te})}{2}. \quad (9.4)$$

Hence, F_{id-si} is also known. Since

$$F_{te-si} + F_{te-id} + F_{te-ed} = 1, \quad (9.5.1)$$

and by symmetry,

$$F_{te-id} = F_{te-ed}, \quad (9.5.2)$$

$$F_{te-id} = \frac{(1-F_{te-si})}{2}. \quad (9.6)$$

Hence, F_{id-te} is also known. Since

$$F_{id-ed} + F_{id-te} + F_{id-si} = 1, \quad (9.7)$$

and F_{id-si} and F_{id-te} are known from Eqs. (9.4) and (9.6), respectively, F_{id-ed} is known. The view factor F_{id-1oK} is obtained by the view factor algebra suggested by Rea [20] as

$$F_{id-1oK} = F_{id-(1o1+1o2+\cdots+1o[K-1]+1oK)} - F_{id-(1o1+1o2+\cdots+1o[K-1])}, \quad (9.8)$$

where the terms in the brackets represent the sums of elemental surfaces to form a continuous surface. Similarly, the view factor F_{id-2iK} is obtained as

$$F_{id-2iK} = F_{id-(2i1+2i2+\cdots+2i[K-1]+2iK)} - F_{id-(2i1+2i2+\cdots+2i[K-1])}. \quad (9.9)$$

The view factor $F_{1oK-2iK'}$ is the same as that for configuration C-93 in [16] as shown in Tso and Mahulikar [18] for which an analytical expression is provided, and the view factor $F_{2iK-2iK'}$ is analytically derived in [19]. Thus the view factors for all the required configurations are known.

Due to the coupling of coolant flow with heat transfer in the annular microchannel, the integral form of the momentum equation given below is included to close the system.

$$\Delta P_{lv} = (\rho_{cl}-\rho_v)\cdot L_r\cdot g\cdot\sin\theta + f_{cl}\left(\frac{\rho_{cl}\cdot V_{cl}^2}{2}\right)\left(\frac{L_r}{D_h}\right) + f_v\cdot\left(\frac{\rho_v\cdot V_v^2}{2}\right) \times \left(\frac{L-L_r}{D_h}\right), \quad (10.1)$$

where the friction factor is of the form [15]

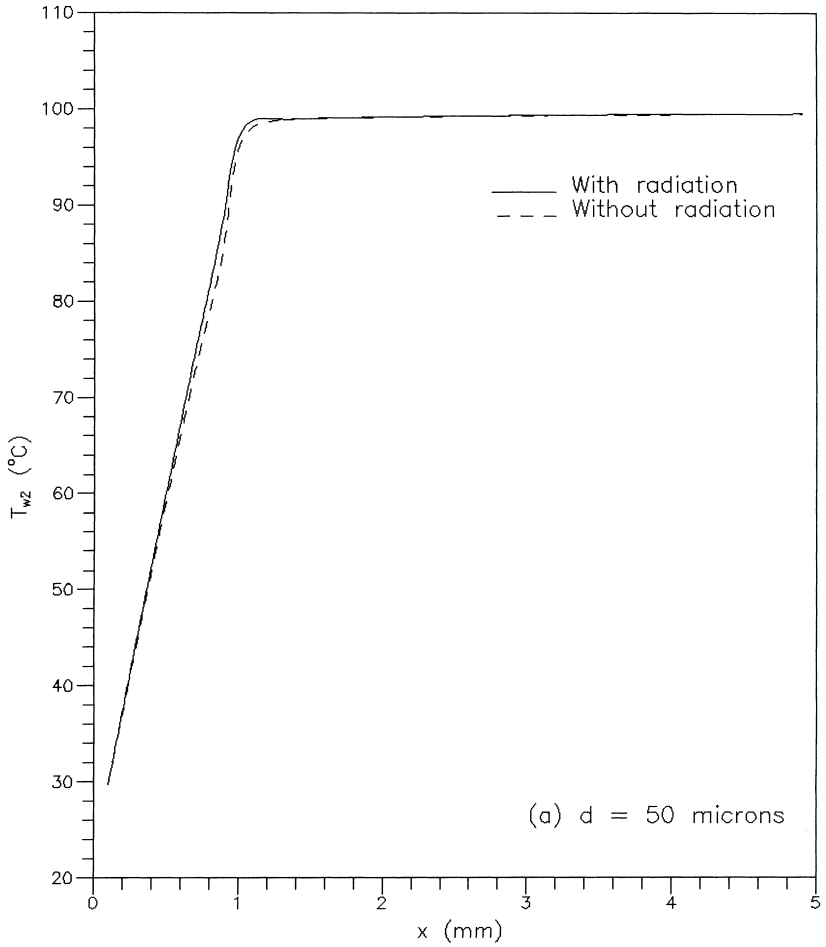

Fig. 5. Temperature distribution with and without surface radiation interchange. (a) $d = 50$ μm, (b) $d = 10$ μm, (c) $d = 5$ μm, (d) $d = 1$ μm, (e) $d = 0.5$ μm.

$$f = C_f/Re^{1.98} \approx C_f/Re^2. \tag{10.2}$$

From Eqs. (10) and (10.1), it is seen that L_r is obtained solely from the integral form of the momentum equation. However, if the value of L_r thus obtained exceeds L, then $L_r = L$, because the coolant cannot overflow, since in an attempt to do so its curvature reduces, thereby reducing the driving force. The coolant mass flow rate, $\dot{m}_{cl}$, which appears in Eq. (6.2), is obtained from

$$\dot{m}_{cl} = \frac{\int_o^{L_r} \left(\dot{q}''_{cv1o} \cdot dA_{1o} + \dot{q}''_{cv2i} \cdot dA_{2i}\right)}{C_{cl}\left(T_{cl,sat} - T_{cl,in}\right) + L_H}, \tag{11}$$

which in turn is obtained by an energy balance from the inlet to the coolant rise length. The C_{cl} in Eq. (11) is obtained at $(T_{cl,sat} + T_{cl,in})/2$. The fluid thermophysical properties are obtained on line at the local fluid temperatures by interpolating from the tables in [26]. Thus Eqs. (8.1), (8.2), (10), (11) are four additional equations required in four unknowns: B_{id}, H_{id}, L_r, and $\dot{m}_{cl}$, introduced for closing the system of equations for the discretised elements.

Thus the heat transfer coupled with the annular microchannel fluid flow is modeled by a closed system of $(14N + 4)$ non-linear simultaneous equations in $(14N + 4)$ unknowns.

3. Results and discussions

The above system of non-linear equations is solved numerically by the Newton–Raphson technique for $N = 40$, resulting in a system consisting of 564 non-linear simultaneous equations. The equations and variables are arranged so as to obtain diagonal dominance

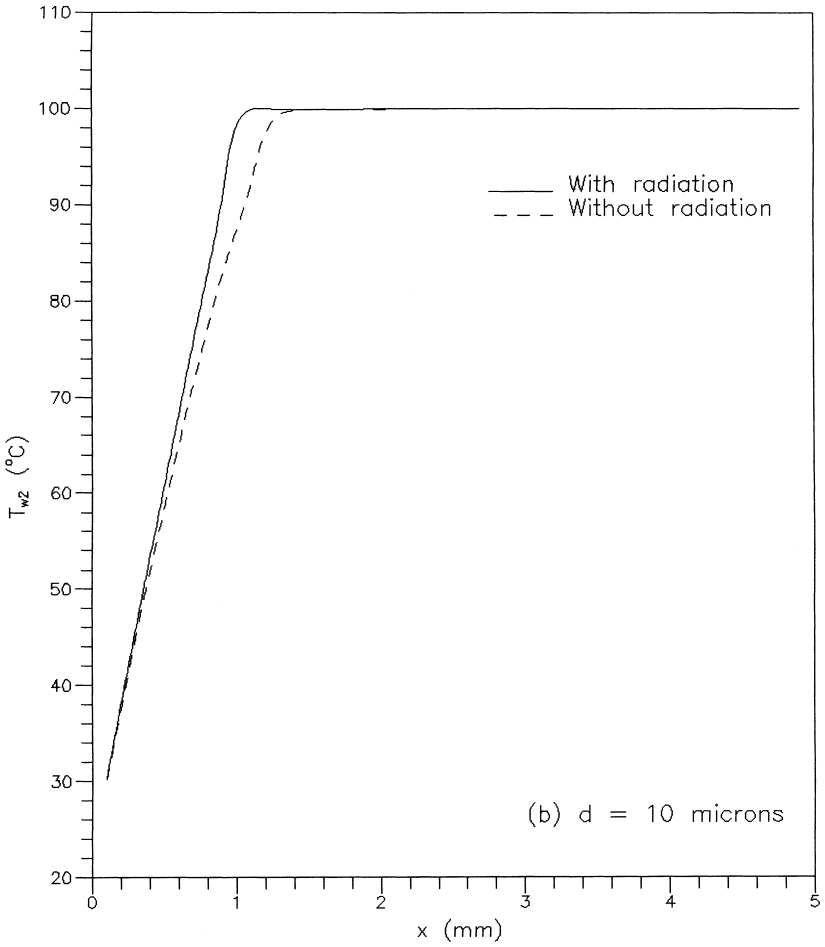

Fig. 5 (*continued*)

of their Jacobian matrix. Hence, the updated values of the variables after iteration can be obtained directly from their values prior to the iteration, without having to solve a system of linear simultaneous equations at the iterations. A computer program is prepared in FORTRAN to simulate the system and to implement the numerical scheme.

To study the system, it is simulated for test cases, whose input data are as follows: Geometry: $L = 8$ mm, $D_{1i} = 1$ cm, $t_1 = 1$ mm, $t_2 = 1$ mm, $\theta = 90^\circ$ (vertical microchannel); Coolants: water in annulus (meniscus-driven), air in core and freestream (V_1, $V_\infty = 0.5$ m/s); Boundary conditions: $T_{a,in} = T_{id} = T_{cl,in} = T_\infty = 15^\circ$C.

The emissivity of all the surfaces participating in radiation, except the black exit disc, is taken as 0.8. The vertical case is chosen as a conservative estimate of the performance, since L_r and $\dot{m}_{cl}$ are the lowest, because the gravity term completely opposes the flow and the rise.

3.1. Effect of surface radiation interchange in microchannels

The effect of surface radiation interchange is likely to be pronounced when there is a large difference in the volume heat generation rates of the two cylinders ($\dot{Q}_1'''$, $\dot{Q}_2'''$). This occurs when there are low and high power ICs packaged together, or if the coolant receives heat only from one of the walls bounding the microchannel. Hence, results are generated with and without the effect of surface radiation interchange, for $\dot{Q}_1''' = 50$ W/cm^3 and $\dot{Q}_2''' = 0$, for which case $L_r > L$, hence $L_r = L$, as discussed earlier. Fig. 5(a–e) give the temperature distributions of cylinder 2 for microchannel spacings $d = 50$, 10, 5, 1, and 0.5 μm, respectively. The results without surface radiation in Fig. 5 are generated by equating the emissivities of the surfaces bounding the annular enclosure to zero (including the emissivity of the end-plugged annular disc at the exit),

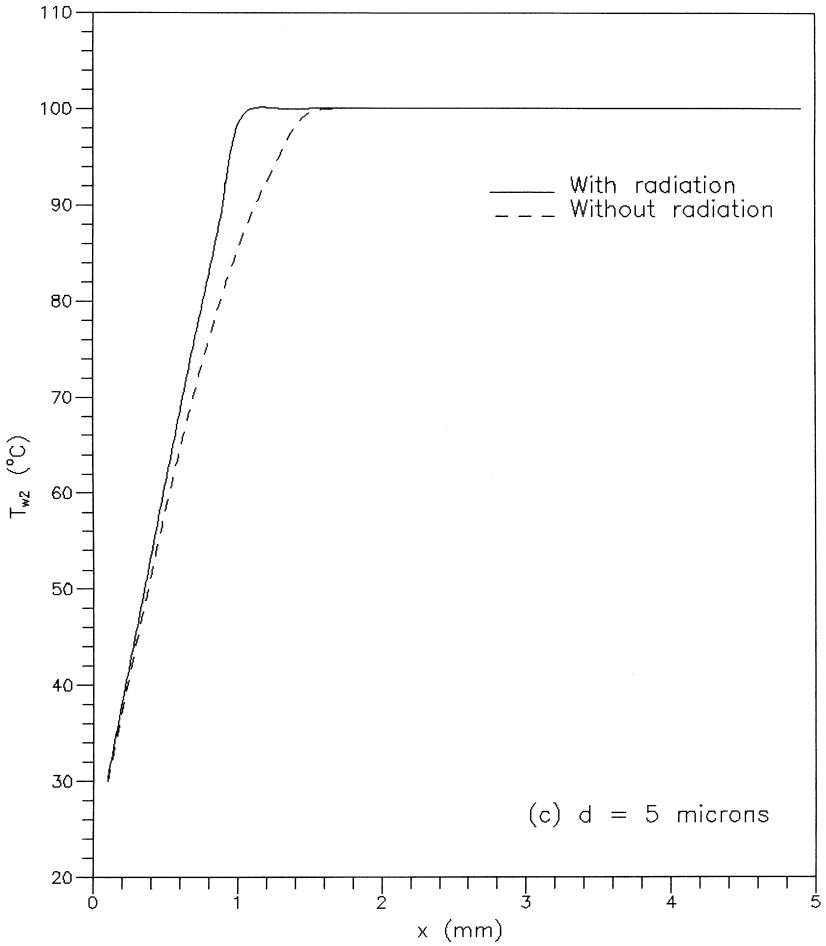

Fig. 5 (*continued*)

and are denoted in the plots by dotted lines. The results indicate that as d is reduced, the T_{w2} temperature variation with and without the effect of radiation significantly differs, as speculated earlier. As is seen, T_{w2} is higher with radiation due to direct heat transfer from cylinder w1 to w2. Table 1 gives the maximum difference in T_{w2} with and without the effect of surface radiation, at the same axial location, for various microchannel spacings. As seen, $\Delta T_{w2,max}$ increases as d reduces. This is because the view factor, $F_{1oK-2iK}$, increases as d reduces. Without radiation, cylinder w2 receives heat from cylinder w1 only through the annulus coolant by convection. This difference becomes pronounced along the length in the region of temperature change of the coolant. The differences in the values are seen to be substantial even for $T_{w2} < 100°C$, i.e., in the temperature change region of the coolant, which are the typical temperatures of the chip for reliable operation. In this range of temperatures, even a temperature change of the order of 10°C can affect the reliability of the system [27]. However, once non-equilibrium phase change begins in the annular microchannel, T_{cl} is fixed, and due to large value of h, T_{w2} is also fixed to a value close to $T_{cl,sat}$. It is noteworthy that the effect of surface radiation interchange is pronounced in spite of the high value of h in the microchannel and the low temperatures. Hence, the effect of surface radiation interchange also affects the variation of T_{cl} and T_{w1}, since they closely follow each others variation due to the large value of h.

3.1.1. Indication of continuum assumption

The computations have been performed up to $d = 0.5$ μm. The mean free path for the liquid molecules required for calculating Kn is not available in the literature. Hence, the liquid molecules are assumed to be arranged at the corners of a cubical lattice like a typical crystalline solid, and the intermolecular distance is

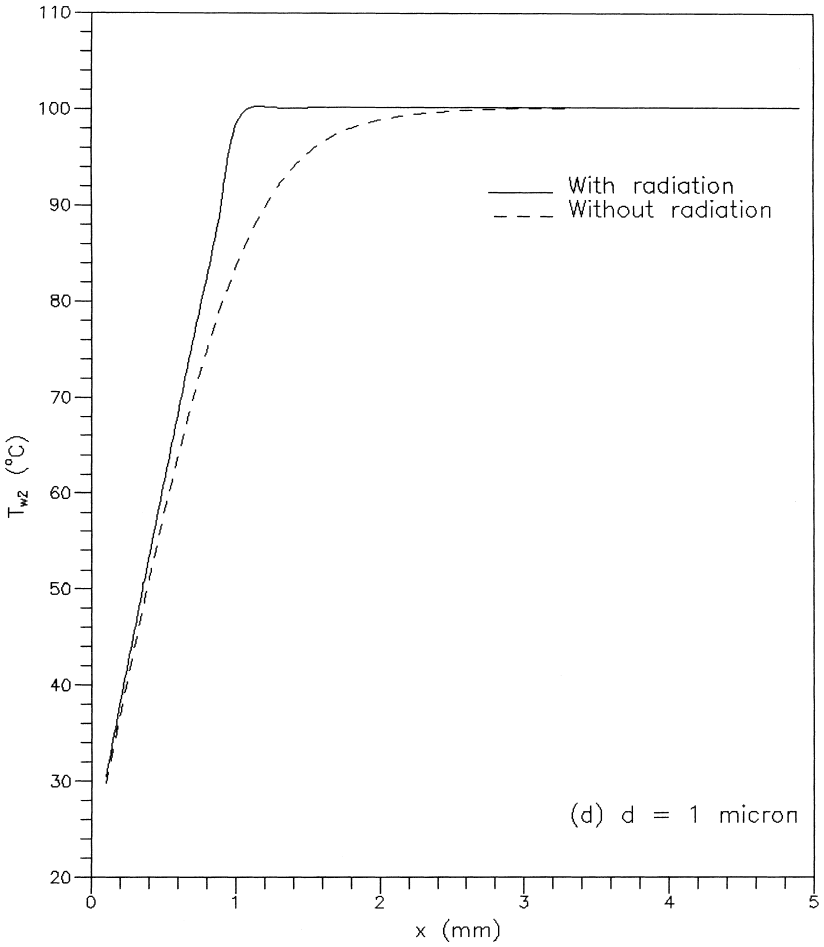

Fig. 5 (*continued*)

used as a first approximation for the mean free path. The volume associated with a molecule, which is the volume of the lattice, is obtained as:

$$\Omega = \frac{M}{\left(6.023 \times 10^{23}\, \rho_{\mathrm{cl,sat}}\right)}, \tag{12.1}$$

Table 1
Maximum T_{w2} difference ($\Delta T_{w2,max}$), with and without radiation

Case	1	2	3	4	5
d (μm)	50	10	5	1	0.5
$\Delta T_{w2,max}$ (K)	3.3	8.0	10.9	13.2	13.3

from which the mean free path is obtained as

$$\lambda = \Omega^{1/3}. \tag{12.2}$$

The value of λ for saturated water is calculated as $\lambda = 0.31481$ nm ($\Omega = 3.12 \times 10^{-29}$ m^3), and $Kn = 6.2962 \times 10^{-4}$ (for $d = 0.5$ μm). As mentioned in [28], for $Kn \geq 1$, the flow is free-molecular. Furthermore, it is mentioned in [29], that slip at the wall tends to occur at low Reynolds numbers and high Mach numbers. In the present problem, though the Reynolds numbers are low, the Mach numbers are negligible due to the low velocities of the coolant and the high velocity of sound in the liquid. Hence, it may be conservatively assumed that the continuum assumption does not breakdown. Also, calculations for saturated water provide a conservative (higher) value of Kn for water, since the density of the saturated liquid is lowest.

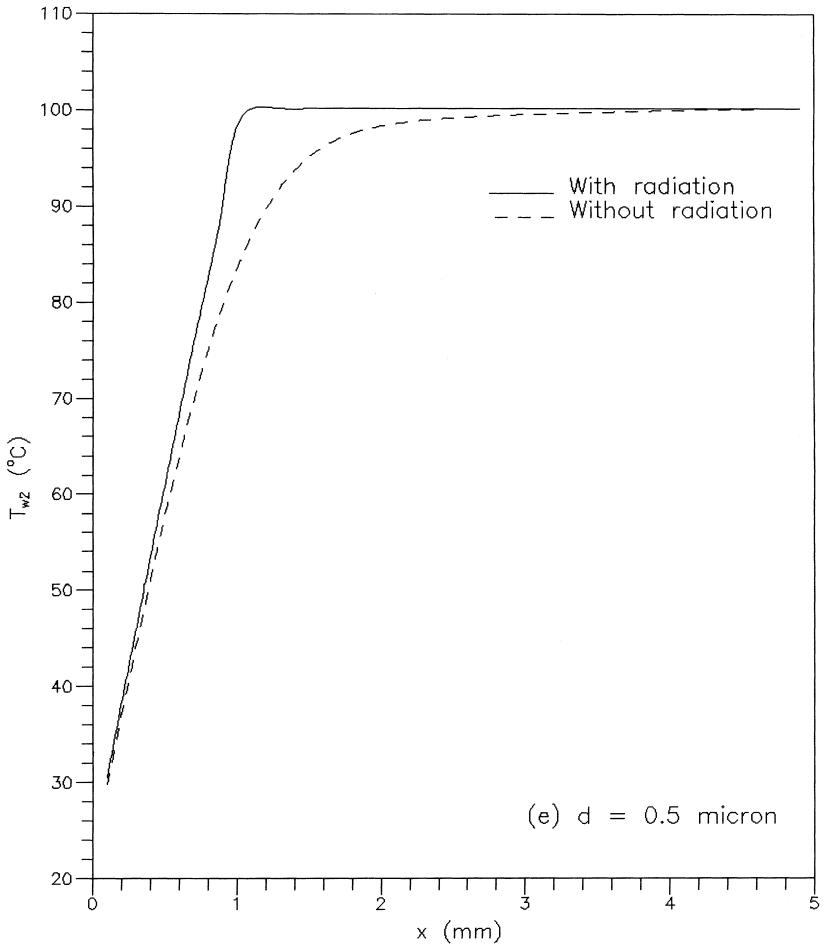

Fig. 5 (*continued*)

Similarly, λ for saturated vapour is calculated as $\lambda = 3.6884$ nm ($\Omega = 3.12 \times 10^{-29}$ m^3), and $Kn = 7.4 \times 10^{-3}$ (for $d = 0.5$ μm), in which case the continuum still hold. However, the λ for a gas is given by the formula [28]

$$\lambda = \frac{1}{\sqrt{2}\pi\phi^2 n}. \tag{12.2}$$

To calculate ϕ, it is assumed that the molecules in the liquid are closely packed relative to its vapour. For this assumption, the Ω calculated above for the saturated liquid is the volume of the molecule (and not the volume associated with a molecule or lattice volume), from which the diameter of the molecule is obtained as $\phi = 3.906 \times 10^{-10}$ m. However, n for saturated water vapour ($n = 1/\Omega = 3.205 \times 10^{28}$ m^{-3}, where $\Omega = 3.12 \times 10^{-29}$ m^3 calculated above) is used. The λ for saturated water vapour is then calculated from Eq. (12.2) as 0.04603 nm, from which $Kn = 9.206 \times 10^{-5}$ (for $d = 0.5$ μm), for which the continuum assumptions do not breakdown.

Hence, it is concluded that the continuum assumptions are highly unlikely to breakdown for the saturated liquid and vapour, for $d \geq 0.5$ μm.

3.2. Results demonstrating self-regulation and phase change

Fig. 6(a) and (b) give the temperature distributions for the same set of input data as before. The objective of presenting these results is only to simulate the heat transfer and flow, downstream of the evaporating meniscus. However, radiation effect is not considered and $d = 100$ μm. Also to demonstrate phase change, $L = 30$ mm, and $L_r = 28$ mm (calculated from the

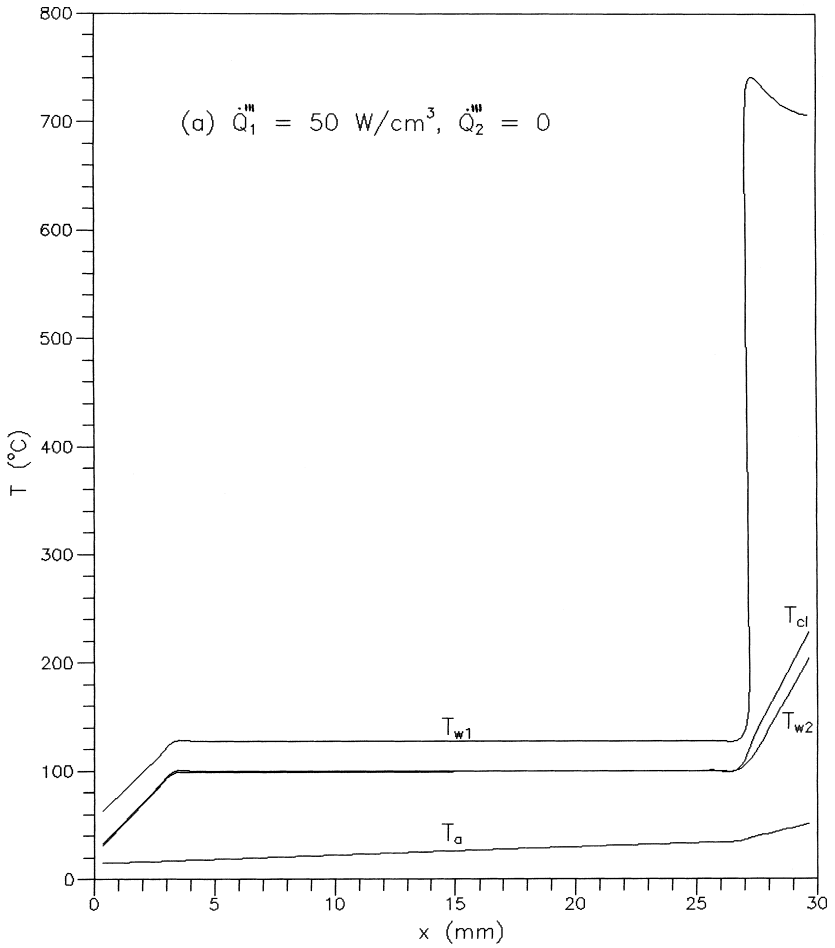

Fig. 6. Temperature distributions. (a) $\dot{Q}_1''' = \dot{Q}_2''' = 50$ W/cm^3, (b) $\dot{Q}_1''' = 50$ W/cm^3 and $\dot{Q}_2''' = 0$.

momentum equation). The results in Fig. 6(a) are for $\dot{Q}_1''' = \dot{Q}_2''' = 50$ W/cm^3, and those in Fig. 6(b) are for $\dot{Q}_1''' = 50$ W/cm^3 and $\dot{Q}_2''' = 0$. Since in the former case only one cylinder generates heat, the value of $\dot{m}_{cl} = 17.26$ mg/s whereas in the latter case, $\dot{m}_{cl} = 38.14$ mg/s, which demonstrates that for a fixed L_r, $\dot{m}_{cl}$ increases as the heat dissipation requirement increases. When both the cylinders generate heat, their temperatures are nearly the same, but when cylinder w2 is off, its temperature is determined by the coolant temperature. In both these figures, the temperature jump after the complete latent heat is added, in the isothermal region, is due to the vapour, whose density and thermal conductivity, and hence cooling capacity are much lower than the liquid. Also the temperature differences between the wall and the coolant increase, which indicates that the value of h for the vapour is much lower than that of the liquid, due to lower thermal conductivity of the vapour. These results also bring out the effectiveness of liquid cooling and phase change in microchannels, as compared to cooling by vapour. Hence, for microelectronics cooling application, it is recommended that the system be designed so that there is no vapour flow in the evaporator, i.e., termination of the heat generating microelectronic components at the meniscus.

Fig. 7 shows the variation of $\dot{m}_{cl}$ with $\dot{Q}'''$ (same for both the cylinders), for a fixed d (= 75 μm). As $\dot{Q}'''$ increases, $\dot{m}_{cl}$ also increases almost linearly. This linear variation is attributed to the fixed L_r in microchannels as discussed earlier, and since bulk of the heat generated is transferred to the annular microchannel coolant due to high values of the convective heat transfer coefficients. Hence, as seen from Eq. (11), the linear variation implies that since L_r (the integration range) is fixed, the convective heat fluxes $\dot{q}''_{cv1o}$ and $\dot{q}''_{cv2i}$ vary linearly with $\dot{Q}'''$. Hence, $\dot{m}_{cl}$ adjusts to meet the heat dissipation demands, due to the coupling of heat transfer and coolant flow, thereby demonstrating that the tech-

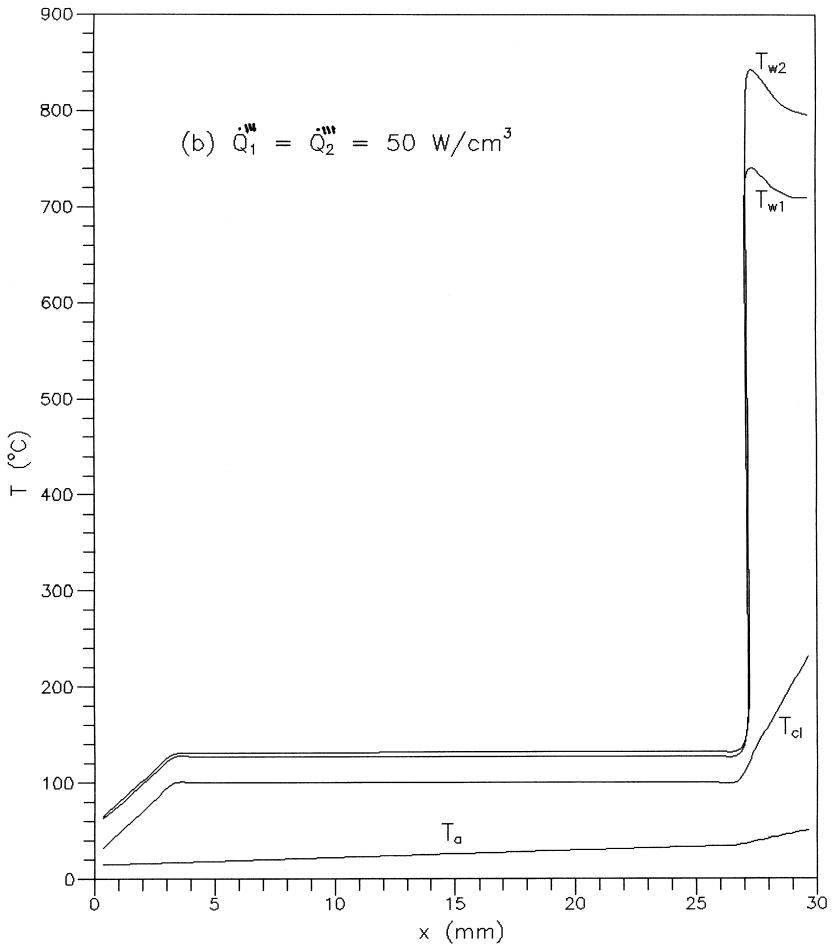

Fig. 6 (*continued*)

nique is self-regulating and hence passive. However, though $\dot{m}_{cl}$ increases with $\dot{Q}'''$, T_w also increases. Hence, the design is acceptable up to heat generation rates such that the chip operating temperatures are lower than the values acceptable for reliable operation.

4. Concluding remarks

The present study has demonstrated the new concept of the evaporating meniscus-driven coolant flow in annular microchannels for application to microelectronics cooling. The results have shown that this technique combines the benefits of high h associated with liquid cooling and phase change in microchannels. The effectiveness of liquid cooling in microchannels as against gas cooling has also been shown (Fig. 6). The technique is shown to be self-regulating. The L_r in microchannels is determined solely by the integral form of the momentum equation. Hence, L_r is independent of $\dot{q}_{cv}''$ supplied to the coolant, but $\dot{m}_{cl}$ adjusts to meet the demands of $\dot{q}_{cv}''$. However, if the typical correlation for the friction factor for a conventionally sized channel were to be used as in the earlier reported literature, L_r would depend on $\dot{q}_{cv}''$. The relative importance of surface radiation interchange among the surfaces bounding the annular microchannel has been brought out as a function of the microchannel spacing even for relatively low temperatures needed for reliable chip operation.

For the concept to be realised in design and for better prediction of its performance, two aspects need to be investigated. Firstly, in the momentum equation, the value of C_f (Eq. (10.2)) is not known for annular microchannels and warrants further investigation. Secondly, the driving force for the coolant flow (ΔP_{lv}

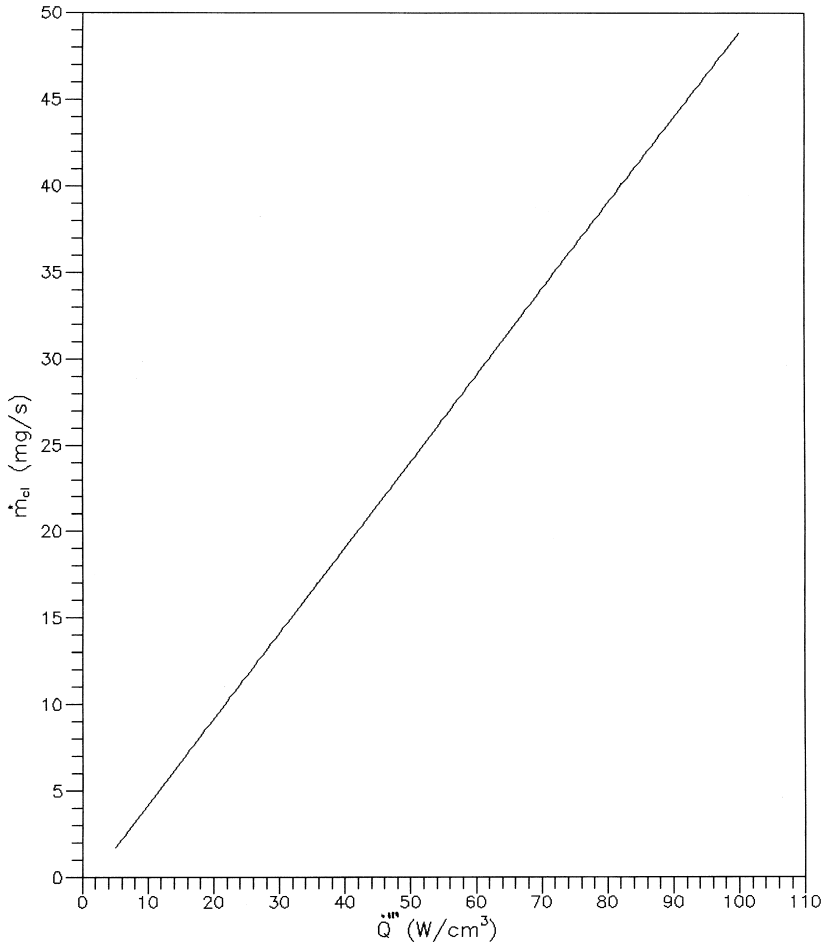

Fig. 7. Illustration of self-regulation.

in Eq. (10)) considers only the curvature of the meniscus (the intrinsic meniscus). Since the meniscus also comprises of the non-equilibrium-evaporating meniscus and the equilibrium non-evaporating meniscus, jointly termed the extended meniscus, they may add to the driving force. The flow and heat transfer in the extended meniscus should be coupled with the flow and heat transfer in the rise length. Furthermore, when the non-equilibrium thermodynamics of phase change in microchannels is better understood analytically, the phase change model should be refined.

References

[1] A. Bar-Cohen, State of the art and trends in the thermal packaging of the electronic equipment, Journal of Electronic Packaging 114 (1992) 257–270.

[2] H. Kristiansen, M. Gulliksen, Flow boiling heat transfer of electronic chips in horizontal channels, Journal of Electronics Manufacturing 5 (1995) 153–164.

[3] M. Misale, A.E. Bergles, Influence of channel width on natural convection and boiling heat transfer from simulated microelectronic components, Experimental Thermal and Fluid Science 14 (1997) 187–193.

[4] X.F. Peng, B.X. Wang, Forced convection and flow boiling heat transfer for liquid flowing through microchannels, International Journal of Heat and Mass Transfer 36 (1993) 3421–3427.

[5] X.F. Peng, B.X. Wang, G.P. Peterson, H.B. Ma, Experimental investigation of heat transfer in flat plates with rectangular microchannels, International Journal of Heat and Mass Transfer 38 (1995) 127–137.

[6] X.F. Peng, H.Y. Hu, B.X. Wang, Boiling nucleation during liquid flow in microchannels, International Journal of Heat and Mass Transfer 41 (1998) 101–106.

[7] S. Moosman, G.M. Homsy, Evaporating menisci of wetting fluids, Journal of Colloid and Interface Science 73 (1980) 212–223.

[8] S. Dasgupta, J.A. Schonberg, I.Y. Kim, P.C. Wayner Jr, Use of the augmented Young–Laplace equation to model equilibrium and evaporating extended menisci, Journal of Colloid and Interface Science 157 (1993) 332–342.
[9] K.P. Hallinan, H.C. Chebaro, S.J. Kim, W.S. Chang, Evaporation from an extended meniscus for nonisothermal interfacial conditions, Journal of Thermophysics and Heat Transfer 8 (1994) 709–716.
[10] C.P. Tso, S.P. Mahulikar, A simulation of evaporating meniscus-driven flow for application to electronics cooling design, Journal of Electronics Manufacturing 6 (1996) 231–241.
[11] D.B. Tuckermann, R.F. Pease, Optimized convective cooling using micromachined structure, Journal of the Electrochemical Society 129 (1982) C98.
[12] C.P. Tso, S.P. Mahulikar, Coupled fluid flow and heat transfer due to an evaporating meniscus in annular microchannels, in: Proceedings of the Seventh Asian Congress of Fluid Mechanics, Chennai, India, vol. 2, 1997, pp. 757–760.
[13] C.P. Tso, S.P. Mahulikar, Semi-analytical study of coupled heat transfer and fluid flow due to evaporating meniscus in annular microchannels for electronics cooling, in: Proceedings of the Second International Seminar on Fluid Mechanics and Heat Transfer, Dhaka, Bangladesh, 1997, pp. 9–16.
[14] C.P. Tso, S.P. Mahulikar, Numerical simulation of coupled flow and evaporating meniscus-driven convection in annular microchannels for electronics cooling, in: Proceedings of the Third High Performance Computing Asia Conference, Singapore, 1998, pp. 732–739.
[15] X.F. Peng, G.P. Peterson, B.X. Wang, Frictional flow characteristics of water flowing through rectangular microchannels, Journal of Experimental Heat Transfer 7 (1994) 249–264.
[16] J.R. Howell, A Catalog of Radiation Configuration Factors, McGraw-Hill, New York, 1982.
[17] R.L. Reid, J.S. Tennant, Annular ring view factors, AIAA Journal 11 (1973) 1446–1448.
[18] C.P. Tso, S.P. Mahulikar, View factor for ring elements on coaxial cylinders, Journal of Thermophysics and Heat Transfer 13 (1999) 155–158.
[19] C.P. Tso, S.P. Mahulikar, View factors between finite length rings on an interior cylindrical shell, Journal of Thermophysics and Heat Transfer 13 (1999) 375–379.
[20] S.N. Rea, Rapid method for determining concentric cylinder radiation view factors, AIAA Journal 13 (1975) 1122–1123.
[21] H. Brockmann, Analytic angle factors for the radiant interchange among the surface elements of two concentric cylinders, International Journal of Heat and Mass Transfer 37 (1994) 1095–1100.
[22] W. Adamson, Physical Chemistry of Surfaces, Wiley, New York, 1990, p. 12.
[23] H. Glaser, Heat transfer and pressure drop in heat exchangers with laminar flow, MAP Volkenrode MAP-VG-96-818T (1947).
[24] B.X. Wang, X.F. Peng, Experimental investigation on liquid forced-convection heat transfer through microchannels, International Journal of Heat and Mass Transfer 37 (1994) 73–82.
[25] F.P. Incropera, D.P. DeWitt, Introduction to Heat Transfer, Wiley, New York, 1990, p. 365.
[26] J.P. Holman, Heat Transfer, 7th ed, McGraw-Hill, London, 1990, p. 663.
[27] A.D. Kraus, A. Bar-Cohen, Thermal Analysis and Control of Electronic Equipment, McGraw-Hill, New York, 1983, p. 35.
[28] W.G. Vincenti, C.H. Kruger Jr, Introduction to Physical Gas Dynamics, Wiley, New York, 1967.
[29] F.M. White, Viscous Fluid Flow, McGraw-Hill, New York, 1974, p. 92.